applied sciences

MDPI

Article

Modeling, Design and Suspension Force Analysis of a Novel AC Six-Pole Heteropolar Hybrid Magnetic Bearing

Chao Wu and Shanshou Li *

School of Electronic and Information Engineering, Anhui Jianzhu University, Hefei 230009, China
* Correspondence: xlisq79@ahjzu.edu.cn

Abstract: To improve the radial suspension force of heteropolar hybrid magnetic bearing (HMB), a novel AC six-pole heteropolar HMB is proposed. Firstly, the structure, magnetic circuit, and suspension force generation principle are introduced and analyzed. Secondly, the equivalent magnetic circuits are established. The mathematical models of magnetic resistances, air gap magnetic fluxes, and levitation force are derived by node magnetomotive force (MMF) method. The main parameters of prototype heteropolar HMB, such as outer and inner air-gap length, winding turns, and permanent magnets, are designed. Then, the analysis model is established by MagNet 3D. The magnetic circuit, air-gap flux density, suspension mechanism, force-current relationships, force-displacement relationships, and force coupling characteristics are analyzed and calculated. Finally, the experimental system was built to test the levitation force and levitation displacement waveforms. The research results have shown that the proposed novel six-pole heteropolar HMB has a reasonable structure and magnetic circuit. The design method is also proven to be correct. Furthermore, it is compared with the traditional heteropolar six-pole HMB, the maximum suspension forces in the X and Y directions are increased by 1.96 and 2.02 times, respectively.

Keywords: heteropolar hybrid magnetic bearing; suspension force; finite element analysis; mathematical model; design

Citation: Wu, C.; Li, S. Modeling, Design and Suspension Force Analysis of a Novel AC Six-Pole Heteropolar Hybrid Magnetic Bearing. *Appl. Sci.* **2023**, *13*, 1643. https://doi.org/10.3390/app13031643

Academic Editors: Xiaodong Sun, Daniel Villanueva Torres and Antonio Di Bartolomeo

Received: 21 November 2022
Revised: 12 January 2023
Accepted: 23 January 2023
Published: 27 January 2023

1. Introduction

In the past ten years, the development of modern industry has put forward the requirements of higher speed and higher power for machines. However, high-speed machines equipped with mechanical bearings have friction and wear, which limits further improvements in speed and power [1,2]. Although air-bearing and liquid-bearing can greatly reduce bearing friction, theoretically, higher power and speed can be obtained. However, they need to be equipped with a special flow supply devices, which leads to the large volume and complex structure of the high-speed motor system and the inevitable problems of air and liquid leakage.

Thanks to magnetic bearings (MBs), in which electromagnetic force is generated to suspend the rotor. Therefore, compared with mechanical bearing, air-bearing, and liquid-bearing, MBs have the advantages of no friction and wear, no lubrication and sealing, long life and maintenance free [3–5]. The high-speed rotor supported by MBs instead of other bearings can easily obtain higher speed and higher power. In addition, compared with bearingless motors such as bearingless permanent magnet motors [6] and bearingless flux-switching permanent motors [7], the combined structure has obvious advantages in terms of simple control and small coupling [8]. They have received extensive attention in the past few decades throughout the world [9–11]. Scholars at home and abroad have developed many kinds of MBs. According to the mechanism of the suspension force producing, MBs can be divided into passive magnetic bearing (PMB) [12], active magnetic bearing (AMB) [13], and hybrid magnetic bearing (HMB) [14]. In particular, the HMB adopts high-performance permanent magnets to balance the rotor. If the rotor deviates from the

balance position, the suspension windings need to be energized to pull the rotor back. Thus, the HMB has a large suspension force density, small volume, and low power consumption. Therefore, HMBs and their applications have become an international hotspot. In [15], an HMB was used in a ring-type flywheel and provided several advantages, such as low energy consumption, good heat dissipation, and linear magnetic force. Reference [16] proposed an AC radial-axial HMB and applied it in a wind energy generation system with running stability and excellent performance. In addition, according to the realized functions, the HMBs are also divided into an axial single degree of freedom (DOF) HMB [17], radial 2-DOF HMB [18], and 3-DOF HMB [19]. Especially, the radial 2-DOF HMB can generate the suspension forces to suspend the rotor in radial 2-DOF, which is often adopted as part of the magnetic suspension motor. At present, radial 2-DOF HMBs mainly include radial three-pole AC HMB, six-pole AC HMB, and four-pole DC HMB [20]. Compared with DC for four-pole HMB and AC three-pole HMB, the AC six-pole HMB not only has the advantages of a symmetrical structure but also can be driven by the three-phase inverter with small volume, low cost and low power consumption [21–25]. Furthermore, according to the bias magnetic circuit, radial HMBs can be divided into homopolar HMBs and heteropolar HMBs [26,27]. In [28], a novel homopolar HMB was put forward to reduce the magnetic field coupling, and the magnetic fields of X and Y channels decoupled well from each other. However, the homopolar HMB has a long axial length because the permanent magnets are usually located in the axial space, which limits the further increase of critical speed. The permanent magnets of the heteropolar HMB are usually installed in the radial space, which has the advantages of short axial length, high critical speed, and high suspension force density [29,30]. Reference [31] proposed one novel heteropolar radial HMB with low rotor core loss. The rotor core loss is just 22.53 W, which is only 41.6% of the conventional one. However, the permanent magnets occupy the stator space, and the area of the magnetic pole decreases, further reducing the levitation force.

In this paper, to increase the levitation forces of heteropolar HMB, a novel AC six-pole heteropolar HMB is proposed. It has the characteristics that the permanent magnets are installed in the radial space, and the double air gaps are adopted. Firstly, the structure and suspension mechanism are analyzed. Secondly, the equivalent magnetic circuits are established. The mathematical models of suspension force are deduced by node magnetomotive force method. Then, the design method of the main parameters is discussed. The electromagnetic performances are calculated by MagNet 3D. The magnetic circuit, suspension mechanism, mathematical models, and design method are proven to be correct. Finally, the closed-loop control system is established. The rotor stable suspension is realized by using STM 32H743 controller. The displacement waveforms in the stable suspension state and anti-disturbance waveform are tested. Compared with the suspension force of the traditional heteropolar HMB, the maximum suspension forces in the X and Y directions are increased by 1.96 and 2.02 times, respectively.

2. Configuration and Suspension Principle

The proposed novel AC six-pole heteropolar HMB includes an inner stator core, outer stator core, permanent magnets, control coils, and rotor. Figure 1 shows the three-dimensional structure and magnetic circuit diagrams. Six magnetic poles denote as A, a, B, b, C, and c, are evenly distributed on the outer stator. Three magnetic poles, a, b and c, extend inward and are connected with cores X, Y and Z by six magnets to form a circular inner stator core. The inner stator core is divided into six poles by six magnets. As a result, there are an annular inner air gap and three outer air gaps. Ignoring the leakage flux, the equivalent magnetic circuit can be obtained. The blue lines denote the control fluxes, and the red lines describe the bias fluxes. It can be seen that one part of the bias fluxes generated by the six magnets passes through the outer air gap, the other parts pass through the inner air gap, and form two closed paths. The coils W_1 and W_4, W_2 and W_5, and W_3 and W_6 of poles A and b, B and c, and C and a are respectively connected in series as $W_{1,4}$, $W_{2,5}$, and $W_{3,6}$. Then, Y-type connection is conducted to get three-phase symmetrical control

windings. One three-phase inverter is adopted to electrify the three-phase windings. It is found that the control fluxes generated by coils W_1, W_3, and W_5 need to pass through the outer and inner air gaps. However, the control fluxes generated by coils W_2, W_4, and W_6 only need to pass through the inner air gaps. Assuming that the rotor has the displacement to the pole b, the three-phase symmetrical currents $i_{w1,4} = -2i_{w2,5} = -2i_{w3,6}$ flow into three-phase windings. As a result, the air gap flux density increases under poles A, a, and c while decreasing under poles b, B, and C. Thus, the suspension force pointing to pole A will pull the rotor back to the balance position.

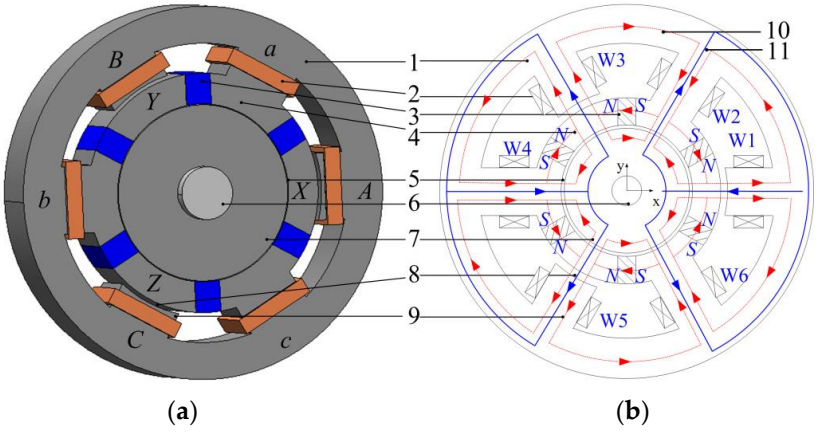

Figure 1. Structure and magnetic circuit of novel AC 6-pole heteropolar HMB, 1—external stator core, 2—control windings, 3—magnets, 4—internal stator core, 5—inner air gap, 6—shaft, 7—rotor core, 8—outer air gap, 9—stator magnetic poles, 10—bias fluxes, 11—control fluxes. (**a**) Three-dimensional structure diagram; (**b**) Magnetic circuit diagram.

3. Mathematical Models

Only the air gap reluctances and the magnet reluctances are considered, and other nonlinear factors are ignored. According to the magnetic circuit and the suspension mechanism, the equivalent magnetic circuits are shown in Figure 2. ϕ_{CR1}~ϕ_{CR6} represent control fluxes of inner air gaps, while ϕ_{PR1}~ϕ_{PR6} are bias fluxes of inner air gaps. ϕ_{PRA}~ϕ_{PRC} represents bias fluxes of outer air gaps. In Figure 2, it is assumed that the magnetomotive force (MMF) of the outer circle is 0. F_m and R_m are the MMF and reluctance of each magnet, respectively. F_1~F_4 are the MMF of four nodes, as shown in Figure 2b.

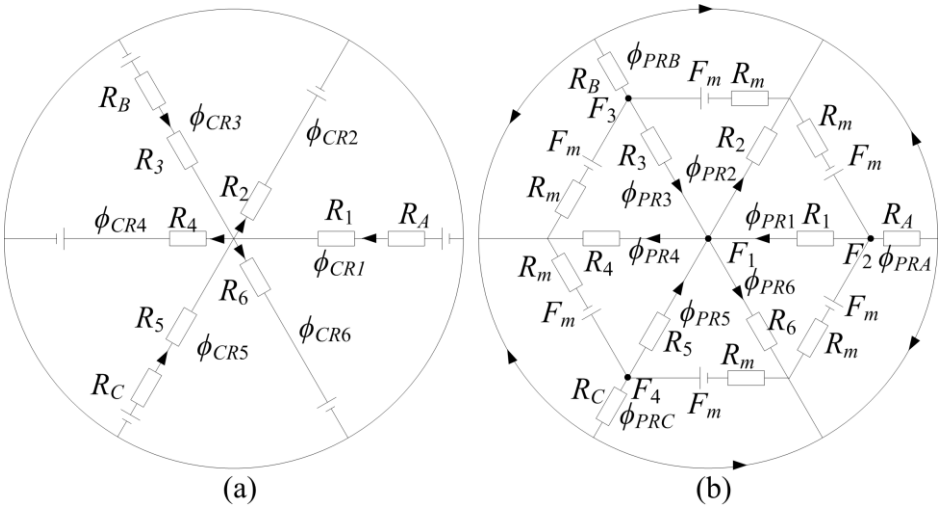

Figure 2. The equivalent magnetic circuit, (**a**) The equivalent control magnetic circuit, (**b**) The equivalent bias magnetic circuit.

Based on the magnetic circuit Kirchhoff's laws, the magnetic circuit equations are derived by node magnetomotive force method.

$$\begin{bmatrix} Q_1 & -\frac{1}{R_1} & -\frac{1}{R_3} & -\frac{1}{R_5} \\ -\frac{1}{R_1} & Q_2 & 0 & 0 \\ -\frac{1}{R_3} & 0 & Q_3 & 0 \\ -\frac{1}{R_5} & 0 & 0 & Q_4 \end{bmatrix} \times \begin{bmatrix} F_1 \\ F_2 \\ F_3 \\ F_4 \end{bmatrix} = \begin{bmatrix} 0 \\ \frac{2F_m}{R_m} \\ \frac{2F_m}{R_m} \\ \frac{2F_m}{R_m} \end{bmatrix} \tag{1}$$

$$\begin{cases} Q_1 = \frac{1}{R_1} + \frac{1}{R_2} + \frac{1}{R_3} + \frac{1}{R_4} + \frac{1}{R_5} + \frac{1}{R_6} \\ Q_2 = \frac{2}{R_m} + \frac{1}{R_1} + \frac{1}{R_A} \\ Q_3 = \frac{2}{R_m} + \frac{1}{R_3} + \frac{1}{R_B} \\ Q_4 = \frac{2}{R_m} + \frac{1}{R_5} + \frac{1}{R_C} \end{cases} \tag{2}$$

Reluctances of the inner and outer air gap can be expressed as

$$R_i = R_j = \frac{g_i}{\mu_0 S_i}, j = 1, 2, 3, 4, 5, 6 \tag{3}$$

$$R_o = R_A = R_B = R_C = \frac{g_o}{\mu_0 S_o} \tag{4}$$

where μ_0 is the permeability of vacuum, S_i is the internal magnetic pole area, g_i is the average inner air-gap length, S_o is the outer magnetic pole area, and g_o is the outer air-gap length.

The bias fluxes of inner air gaps can be expressed as

$$\begin{cases} \phi_{PR1} = \frac{F_2 - F_1}{R_1} \\ \phi_{PR2} = \frac{F_1}{R_2} \\ \phi_{PR3} = \frac{F_3 - F_1}{R_1} \\ \phi_{PR4} = \frac{F_1}{R_4} \\ \phi_{PR5} = \frac{F_4 - F_1}{R_1} \\ \phi_{PR6} = \frac{F_1}{R_6} \end{cases} \tag{5}$$

The control fluxes of inner air gaps can be written as

$$\begin{cases} \phi_{CR1} = \frac{N_o i_A}{R_1 + R_A} \\ \phi_{CR2} = \frac{N_i i_C}{R_2} \\ \phi_{CR3} = \frac{N_o i_B}{R_3 + R_B} \\ \phi_{CR4} = \frac{N_i i_A}{R_4} \\ \phi_{CR5} = \frac{N_o i_C}{R_5 + R_C} \\ \phi_{CR6} = \frac{N_i i_B}{R_6} \end{cases} \tag{6}$$

where N_o represents the turn numbers of coils W_1, W_3, and W_5, and N_i represents the turn number of coils W_2, W_4, and W_6.

The magnetic attraction force of poles a-C, A-b, and c-B to the rotor can be given as follows.

$$\begin{cases} F_{aC} = \frac{\left(\phi_{PR2} + \phi_{CR2}\right)^2 - \left(\phi_{PR5} - \phi_{CR5}\right)^2}{2\mu_0 S_i} \\ F_{Ab} = \frac{\left(\phi_{PR1} + \phi_{CR1}\right)^2 - \left(\phi_{PR4} - \phi_{CR4}\right)^2}{2\mu_0 S_i} \\ F_{cB} = \frac{\left(\phi_{PR6} + \phi_{CR6}\right)^2 - \left(\phi_{PR3} - \phi_{CR3}\right)^2}{2\mu_0 S_i} \end{cases} \tag{7}$$

According to the equivalent magnetic circuit, then the maximum suspension forces in radial 2-DOF can be deduced as

$$\begin{cases} F_{+x\max} = F_{-x\max} = \frac{3B_s^2 S_i}{2\mu_0} \\ F_{+y\max} = F_{-y\max} = \frac{\sqrt{3}B_s^2 S_i}{2\mu_0} \end{cases} \tag{8}$$

where B_s is the saturated flux density. B_0 is bias flux density. F_{+xmax}, F_{-xmax}, F_{+ymax}, F_{-ymax} are the maximum suspension force in +X, $-X$, $+Y$, and $-Y$ directions.

Form Equation (8), it is concluded that the maximum suspension force in the positive X and negative X directions are equal, the suspension force in the negative Y and positive Y directions is equal, and the maximum suspension force in the X direction is greater than that in the Y direction.

4. Parameter Design

In order to avoid magnetic saturation, the inner air gap bias flux is half of the saturation flux, that is $\phi_{PRj} = \phi_{PCj} = \phi_{P0} = \phi_s/2$ (j = 1, 2, 3, 4, 5, 6). Thus, the saturation flux density B_s = 1.2 T, and inner air gap bias flux density B_i = 0.6 T. According to (1)~(5), the relationship between the inner and outer air gap parameters is obtained as follows.

$$\frac{g_i}{S_i} \cdot \frac{S_o}{g_o} = \frac{1}{4} \tag{9}$$

According to equivalent control magnetic circuit, the relationships of the turn numbers of N_o and N_i can be described by

$$N_i = N_o\left(\frac{S_o}{S_o + \frac{g_o S_i}{g_i}}\right) \tag{10}$$

Substituting Equation (9) into Equation (10), it is assumed that the $S_o = S_i$, the relationships between N_i and N_o is given by

$$N_o : N_i = 5 : 1 \tag{11}$$

The turn numbers of suspension winding can be calculated by the following formula.

$$N_i i = \frac{B_s g_i}{4\mu_0} \tag{12}$$

As it is known that the demagnetization curve of NdFeB magnets is almost linear, the magnetomotive force F_m and flux ϕ_m for operating point can be expressed as

$$\begin{cases} F_m = F_c/2 \\ \phi_m = \frac{\phi_r}{F_c} \cdot (F_c - F_m) \end{cases} \tag{13}$$

where F_c and ϕ_r are the coercive magnetomotive force and residual magnetic flux of PM, respectively. ϕ_m is the external magnetic circuit flux of PM.

When the rotor is in the no-load state, the following equations can be obtained.

$$\begin{cases} B_0 = \frac{\mu_0 F_m}{2g_0} \\ \phi_m = B_0 S_i \end{cases} \tag{14}$$

Combining (7), (13), and (14), the height and area of PM can be obtained as

$$\begin{cases} H_{pm} = \frac{F_c}{H_c} = \frac{4B_0 g_i}{\mu_0 H_c} \\ A_{pm} = \frac{\phi_r}{B_r} = \frac{2B_0 S_i}{B_r} \end{cases} \tag{15}$$

where H_{pm} is the length of the permanent magnet, H_c is the coercivity of the permanent magnet, A_{pm} is the sectional area of the permanent magnet, and B_r is the residual magnetic flux density of the permanent magnet.

Therefore, as long as the required maximum suspension force is given, the main parameters of the proposed HMB can be designed according to the above design scheme. In this paper, an HMB with a suspension force of no less than 300 N is designed. Firstly, considering the processing accuracy, suspension winding current, and power consumption, the inner air gap length g_i = 0.5 mm is selected. Thus, from Equation (10), the outer air gap length g_o = 2 mm. In order to make full use of the iron cores, improve the suspension force density, and then reduce the volume of HMB, the air gap saturation flux density B_s = 1.2 T is selected. Therefore, the inner air gap flux density B_0 generated by magnets is 0.6 T, and the inner air gap flux density generated by the suspension currents to obtain the maximum suspension force is also 0.6 T. Thus, from Equation (13), the ampere turns of inner control winding is 238.8 AT. Therefore, the ampere turns 240 AT are required, and the ampere turns of outer control winding is 1200 AT. From Equation (8), the pole area S_i = 302 mm^2.

5. Analyses

According to the above analysis, the main parameters are designed and given in Table 1.

Table 1. Parameters Of Model.

Parameter	Value
Radial inner air gap length	0.5 mm
Radial outer air gap length	2 mm
Outer diameter of rotor	50 mm
Outer diameter of stator	106 mm
Number of outer winding turns	240
Number of inner winding turns	60
Axial length of magnetic pole	45 mm
Outer diameter of PM	68 mm
Inner diameter of PM	50.5 mm
Area of inner magnetic pole	302 mm^2
Air gap bias flux	0.6 T

According to Table 1, the analysis model is established by MagNet 3D. The stator and rotor core is made of silicon steel, and the high-performance NdFeB is used to provide bias magnetic fluxes. To prove the bias magnetic circuit, only the magnets are excited, and the windings are not energized. The bias flux cloud diagram and the magnetic line diagram are obtained as shown in Figure 3a,b. It can be concluded that the bias fluxes pass through the internal and external air gaps respectively which proves the correctness of the bias magnetic circuit design. Furthermore, the flux density waveform of internal air gaps is obtained in Figure 3c. The air gap flux densities under magnetic poles X, Y, Z, a, b, and c are all equal to 0.6T, and the design meets the requirements.

To verify the design of the control magnetic circuits, the control fluxes to generate the maximum suspension forces F_{-xmax} and F_{-ymax} in the −X and −Y directions are simulated. According to the suspension mechanism and design parameters, to generate the maximum levitation force F_{-xmax}, the currents $i_{W1,4}$= −4 A, $i_{W2,5}$ = $i_{W3,6}$ = 2 A are necessary. The control flux distribution is shown in Figure 4a. Then, the control currents $i_{W1,4}$= 0 A, $i_{W2,5}$ = $i_{W3,6}$ = −4 A are electrified to obtain F_{-ymax} in the −Y direction. The control flux distribution is shown in Figure 4b. It can be seen from the two figures that the control fluxes are symmetrically distributed, which is the same as the suspension mechanism.

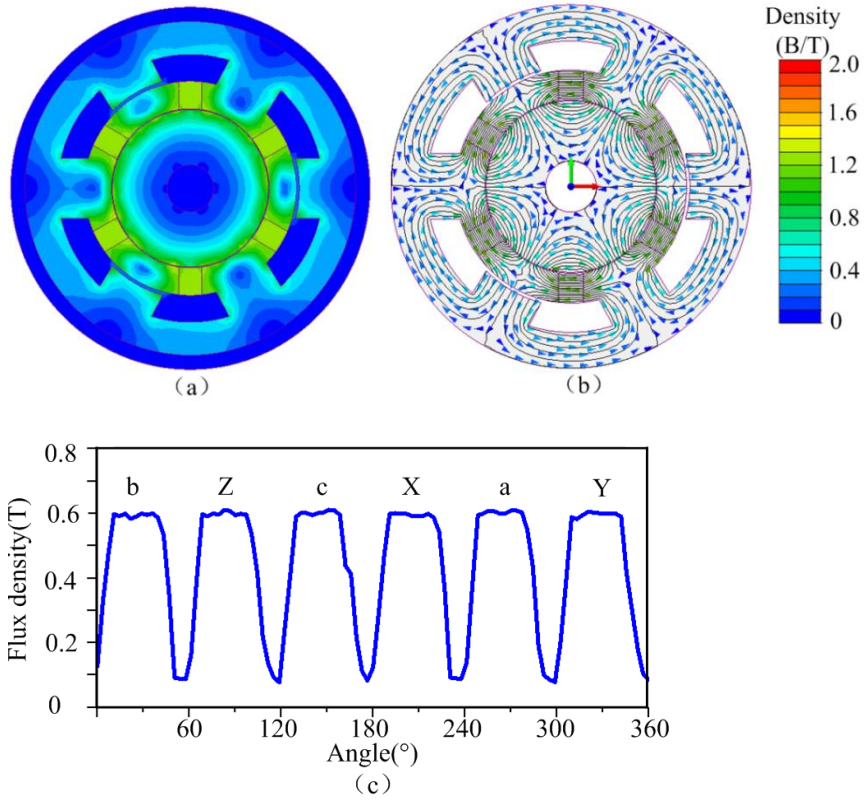

Figure 3. Bias flux. (**a**) The flux cloud diagram; (**b**) The magnetic lines diagram; (**c**) The air gap flux density waveform.

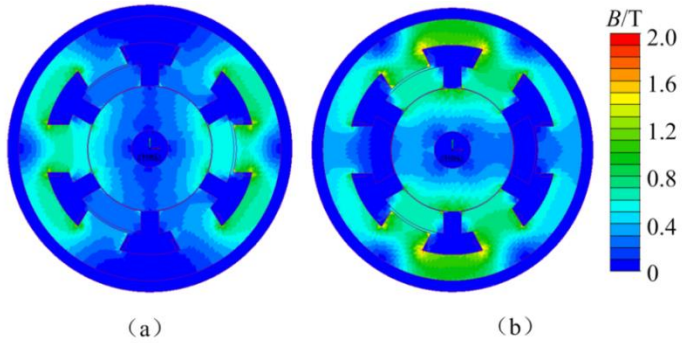

Figure 4. The control flux distribution diagram. (**a**) The flux cloud diagram generating negative $F_{-\mathrm{xmax}}$; (**b**) The flux cloud diagram generating negative $F_{-\mathrm{ymax}}$.

To further verify the suspension mechanism, the control currents under the conditions of Figure 4 are excited together with the magnets. That is, the bias fluxes are superimposed with the control fluxes. The resultant flux distributions under the conditions of generating the maximum suspension forces in the −X and −Y directions are shown in Figure 5, respectively. It can be seen that the control flux breaks the balance of the air gap bias flux, resulting in the increase of the internal air gap flux in the −X and −Y directions, while the internal air gap flux in the opposite direction decreases. Therefore, according to the generation mechanism of Maxwell force, it can be concluded that in these two cases, the suspension force pointing to the −X and −Y directions does occur on the rotor. Furthermore, it can be found that the air gap flux density in the −X and −Y directions basically reaches the maximum value of 1.2 T, while the air gap flux density in the opposite directions is about 0 T. It is further proved that in these two ways, the maximum suspension forces in the −X and −Y directions is indeed produced.

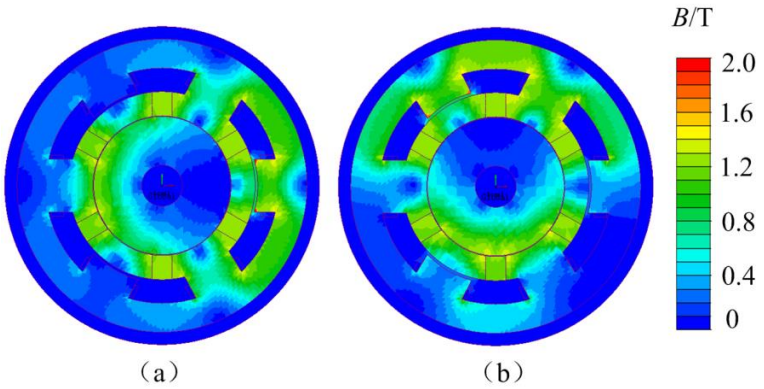

Figure 5. The resultant flux distribution diagrams. (**a**) The resultant flux cloud diagram to generate $F_{-\mathrm{xmax}}$ in the −X direction; (**b**) The resultant flux cloud diagram to generate $F_{-\mathrm{ymax}}$ in the −Y direction.

In order to further analyze the air gap flux density in detail, the air gap control flux density and air gap resultant flux density waveforms are given, as shown in Figure 6. In Figure 6a, curve 1 represents the air gap control flux waveform corresponding to Figure 4a. and curve 2 represents the air gap resultant flux waveform corresponding to Figure 5a. It can be seen that the air gap control flux density at poles *b*, *Z*, *c*, *X*, *a*, and *Y* is 0.6 T, 0.28 T, 0.28T, 0.6 T, 0.28 T, and 0.28 T, respectively. The flux, as shown in curve 1, is added with the bias flux shown in Figure 3c, which will produce a suspension force pointing in the −X direction. It can be seen from curve 2 that the air gap resultant flux densities of poles *b*, *Z*, *c*, *X*, *a*, and *Y* are 1.2 T, 0.9 T, 0.32 T, 0 T, 0.32 T and 0.9 T, respectively. In this case, a suspension force pointing in the −X direction is indeed generated. Similarly, the air gap control flux and resultant flux to generate the suspension force in the −Y direction are calculated, and the waveforms are shown in curve 3 and curve 4 of Figure 6b.

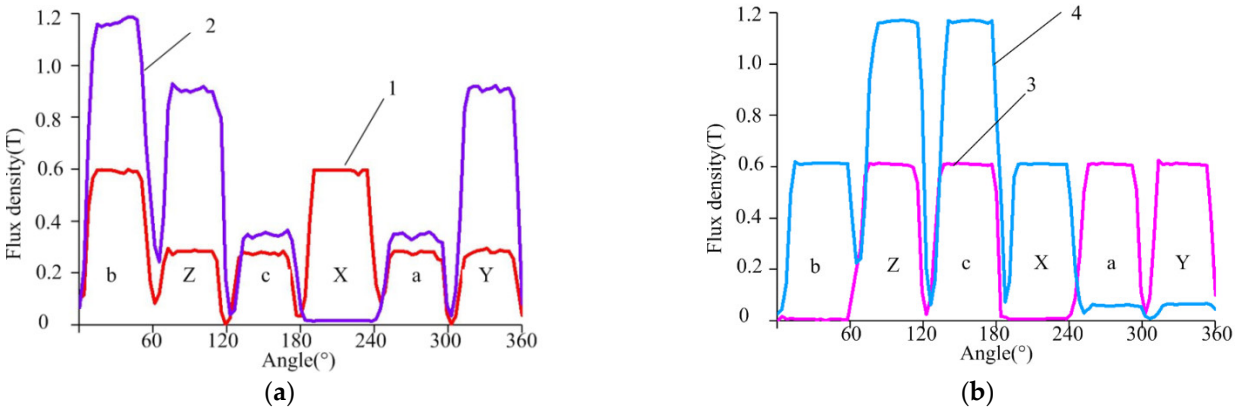

Figure 6. Waveform of the flux density. (**a**) The waveform of the air gap control flux density and resultant air gap flux density to generate $F_{-\mathrm{xmax}}$ in the −X direction; (**b**) The waveform of the air gap control flux density and resultant air gap flux density to generate $F_{-\mathrm{xmax}}$ in the −Y direction.

Figure 7 shows force-current relationships using the parametric analysis method. The currents $i_{w1,4} = -2i_{w2,5} = -2i_{w3,6} = I$ are electrified to the three-phase windings, and I is changing from 0 A to 5 A. The calculation results are shown in Figure 7a. the force F_x is generated, and the force-current relationships are basically linear. When the current is 4A, flux saturation occurs. In this case, the levitation force F_x is 520 N, and the force F_y is always 0 N. In Figure 7b, the currents $i_{w1,4} = 0$ A, $i_{w2,5} = i_{w3,6} = I$ are electrified to the three-phase windings, and I is changing from 0 A to 5 A. It is clear that the force F_y is generated, and when the current is 4 A, saturation has occurred. In this case, the suspension force F_y is 297 N. However, the force F_x is always 0 N. Under the unsaturated condition,

the maximum suspension forces calculated by the finite element method basically coincide with the values calculated according to the Equation (8).

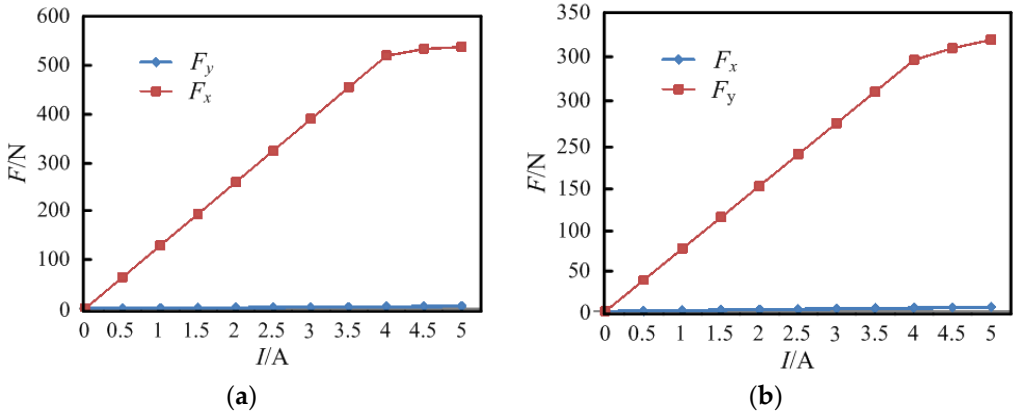

Figure 7. The force-current relationships. (**a**) The relationships of F_x/I and F_y/I when $i_{w1,4} = -2i_{w2,5} = -2i_{w3,6} = I$, and I is changing from 0 A to 5 A; (**b**) The relationships of F_x/I and F_y/I when $i_{w1,4} = 0$ A, $i_{w2,5} = i_{w3,6} = I$, and I is changing from 0 A to 5 A.

The influences of rotor displacements on force-current relationships are calculated, and the results are shown in Figure 8. From Figure 8a, we calculate the curve of F_y/I_y when displacements X are −0.2 mm, −0.1 mm, 0 mm, 0.2 mm, and −0.2 mm, respectively. It can be seen that the curve of F_y/I_y is linear when the rotor has the displacements in the X direction. In other words, the suspension force in the Y direction is not affected by the displacement in the X direction. A similar conclusion can be obtained by analyzing Figure 8b. The air gap length of the HMB designed in this paper is 0.6 mm. In fact, the allowable displacement of the magnetic suspension system is less than one-tenth of the air gap length. Therefore, when the rotor displacement is small, it can be considered that the suspension forces in X and Y directions are uncoupled.

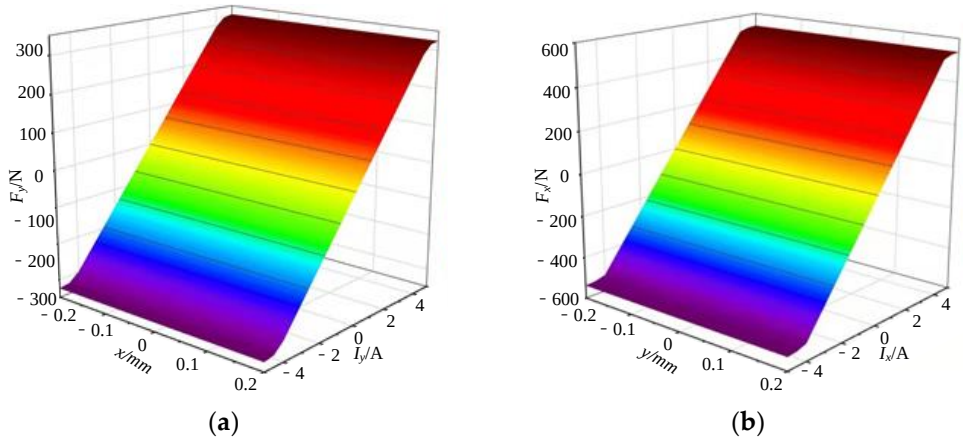

Figure 8. Influence of rotor displacement on force-current relationship. (**a**) The relationships of F_y/I when the displacement x is −0.2 mm, −0.1 mm, 0.1 mm, and 0.2 mm, respectively; (**b**) The relationships of F_x/I when the displacement y is −0.2 mm, −0.1 mm, 0.1 mm and 0.2 mm, respectively.

Finally, we build a prototype according to the design parameters. The STM 32H743 microcomputer and the PID control algorithm are used to realize the stable suspension of the rotor. The control system is shown in Figure 9. First, the current and displacement sensors detect the three-phase currents and radial displacements, respectively. The signals are input to the STM 32H743 microcontroller through the interface circuit for A/D sampling. In STM 32H743, the control algorithm is implemented, and the control signals are

output to three-phase inverter to control winding currents. The magnetic bearing rotor is stably suspended.

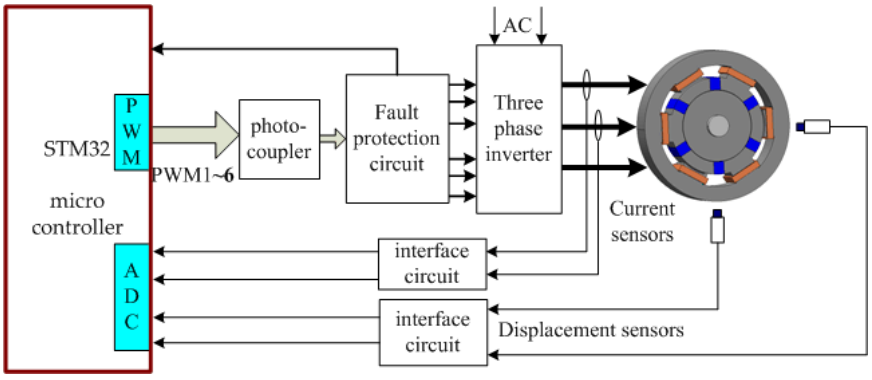

Figure 9. Control system diagram.

Under the no-load condition, the stable suspension displacement waveforms of the rotor are tested, as shown in Figure 10. It can be seen that the proposed HMB can realize the stable suspension of the rotor. Furthermore, the suspension force under the currents of $i_{w1,4} = -2\ i_{w2,5} = -2\ i_{w3,6} = 4$ A is 526 N, while the suspension force under the currents of $i_{w1,4} = 0$ A, $i_{w2,5} = i_{w3,6} = 4$ A is 294 N, which are consistent with the design results. However, the maximum suspension forces of the heteropolar HMB with the same air gap and stator inner diameter designed in an earlier stage is $F_{+ymax} = 150$ N, $F_{+xmax} = 260$ N. The suspension forces are increased by 1.96 times and 2.02 times, respectively. In the stable suspension state, an instantaneous disturbing force in the Y direction is applied to the rotor. The displacement waveform, in this case, is shown in Figure 11. It can be seen that the displacement in the Y direction can quickly again achieve stable suspension after the disturbing force disappears. The control system can respond quickly to the change in rotor displacement.

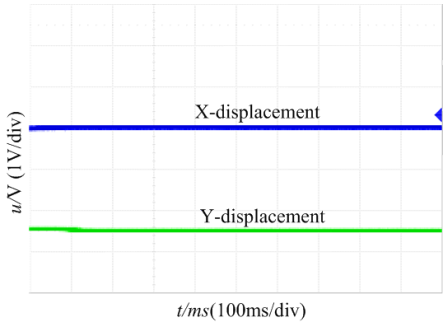

Figure 10. Stable suspension displacement waveform.

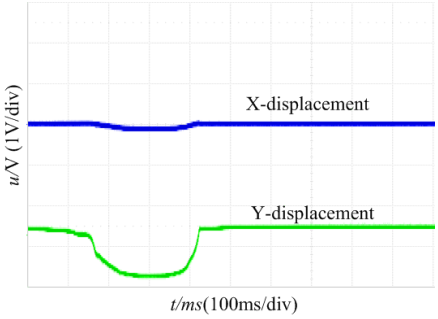

Figure 11. Disturbed displacement waveform.

6. Conclusions

In this paper, a novel AC six-pole HMB is proposed and designed. The conclusions are as follows:

(1) The structure and magnetic circuit of the six-pole HMB studied in this paper are reasonable, and the mathematical models are correct.

(2) The relationship between the suspension force and the current is linear under the condition that the suspension force is not saturated.

(3) When the rotor displacement is small, the levitation forces in X and Y directions are not coupled.

(4) The suspension forces under the currents of $i_{w1,4} = -2$ $i_{w2,5} = -2$ $i_{w3,6} = 4$ A and $i_{w1,4} = 0$ A, $i_{w2,5} = i_{w3,6} = 4$ A are calculated and tested. The finite element results are 297 N and 520 N, respectively. Under the same conditions, the experimentally measured values are 294 N and 526 N, respectively.

(5) Compared with the traditional six-pole heteropolar HMB with the same air gap and stator inner diameter, the suspension forces of the proposed heteropolar HMB are increased by 1.96 times and 2.02 times, respectively.

The theory and experiment have shown that the proposed HMB has good electromagnetic performance. However, the experimental results were obtained in static suspension. Therefore, the focus of the following research is to use this HMB to support the motor rotor and test its suspension performance in the high-speed rotating state.

Author Contributions: Conceptualization, S.L.; writing—review and editing, C.W. All authors have read and agreed to the published version of the manuscript.

Funding: His work was supported by the Project of Anhui Housing and Urban-Rural Construction Science and Technology Planning (grant no. 2022-YF168).

Institutional Review Board Statement: Not applicable.

Informed Consent Statement: Not applicable.

Data Availability Statement: Data are contained within the article.

Conflicts of Interest: The authors declare no conflict of interest.

References

1. Supreeth, D.K.; Bekinal, S.I.; Chandranna, S.R.; Doddamani, M. A review of superconducting magnetic bearings and their application. *IEEE Trans. Appl. Supercond.* **2018**, *32*, 3800215. [CrossRef]
2. Sun, X.; Chen, L.; Yang, Z. Overview of bearingless permanent magnet synchronous motors. *IEEE Trans. Ind. Electron.* **2013**, *60*, 5528–5538. [CrossRef]
3. Tomczuk, B.; Wajnert, D. Field–circuit model of the radial active magnetic bearing system. *Electr. Eng.* **2018**, *100*, 2319–2328. [CrossRef]
4. Debnath, S.; Biswas, P.K. Advanced magnetic bearing device for high-speed applications with an I-type electromagnet. *Electr. Power Compon. Syst.* **2021**, *48*, 1862–1874. [CrossRef]
5. Nielsen, K.K.; Bahl, C.R.H.; Dagnaes, N.A.; Santos, I.F.; Bjørk, R. A passive permanent magnetic bearing with increased axial lift relative to radial stiffness. *IEEE Trans. Magn.* **2021**, *57*, 8300108. [CrossRef]
6. Ren, Y.; Chen, X.; Cai, Y.; Zhang, H.; Xin, C.; Liu, Q. Attitude-rate measurement and control integration using magnetically suspended control and sensitive gyroscopes. *IEEE Trans. Ind. Electron.* **2018**, *65*, 4921–4932. [CrossRef]
7. Shi, Z.; Sun, X.; Lei, G.; Tian, X.; Guo, Y.; Zhu, J. Multiobjective optimization of a five-phase bearingless permanent magnet motor considering winding area. *IEEE/ASME Trans. Mechatron.* **2022**, *27*, 2657–2666. [CrossRef]
8. Sun, X.; Jin, Z.; Wang, S.; Yang, Z.; Li, K.; Fan, Y.; Chen, L. Performance improvement of torque and suspension force for a novel five-phase BFSPM machine for flywheel energy storage systems. *IEEE Trans. Appl. Supercond.* **2019**, *29*, 0601505. [CrossRef]
9. Supreeth, D.K.; BEKINAL, S.I.; Chandranna, S.R. An overview on electrodynamic bearings. *IEEE Access* **2022**, *10*, 57437–57451.
10. Yamagishi, K. Optimum design of integrated magnetic bearing using multiple HTS bulk units. *IEEE Trans. Appl. Supercond.* **2019**, *29*, 6801505. [CrossRef]
11. Hsieh, H.-C.; Nguyen, A.D.; Lai, J.-S. Low noise ZVS switch sharing multichannel switching amplifier for magnetic bearing applications. *IEEE Trans. Circuits Syst.—II Express Briefs* **2020**, *67*, 1999–2003. [CrossRef]
12. Karmakarand, M.; Sarkar, S. Semi-analytical finite element approach for 6-DOF characterizations of PMB load. *IEEE Trans. Magn.* **2022**, *58*, 8001510.

13. Sheh, H.; Zad, T.; Khan, I.; Lazoglu, I. Design and adaptive sliding-mode control of hybrid magnetic bearings. *IEEE Trans. Ind. Electron.* **2018**, *65*, 2537–2547. [CrossRef]
14. Wajnert, D.; Tomczuk, B. Two models for time-domain simulation of hybrid magnetic bearing's characteristics. *Sensors* **2022**, *22*, 1567. [CrossRef]
15. Wei, N.; Qinghai, W.; Defei, J.; Xiaofeng, H.; Tao, Z. Study on measuring and control system of AC radial-axial hybrid magnetic bearing used in wind energy generation system. In Proceedings of the 31st Chinese Control Conference, Hefei, China, 25–27 July 2012; pp. 6847–6850.
16. Wang, H.; Liu, K.; Ao, P. Magnetic field and specific axial load capacity of hybrid magnetic bearing. *IEEE Trans. Magn.* **2013**, *49*, 4911–4917. [CrossRef]
17. Sun, X.; Jin, Z.; Chen, L.; Yang, Z. Disturbance rejection based on iterative learning control with extended state observer for a four-degree-of-freedom hybrid magnetic bearing system. *Mech. Syst. Signal Process* **2021**, *153*, 107465. [CrossRef]
18. Jin, Z.; Sun, X.; Cai, Y.; Zhu, J.; Lei, G.; Guo, Y. Comprehensive sensitivity and cross-factor variance analysis-based multi-objective design optimization of a 3-DOF hybrid magnetic bearing. *IEEE Trans. Magn.* **2021**, *57*, 8000204. [CrossRef]
19. Jin, Z.; Sun, X.; Chen, L.; Yang, Z. Robust multi-objective optimization of a 3-pole active magnetic bearing based on combined curves with climbing algorithm. *IEEE Trans. Ind. Electron.* **2022**, *69*, 5491–5501. [CrossRef]
20. Jiancheng, F.; Jinji, S.; Hu, L.; Jiqiang, T. A novel 3-DOF axial hybrid magnetic bearing. *IEEE Trans. Magn.* **2010**, *46*, 4034–4045. [CrossRef]
21. Sun, X.; Su, B.; Chen, L.; Yang, Z.; Xu, X.; Shi, Z. Precise control of a four degree-of-freedom permanent magnet biased active magnetic bearing system in a magnetically suspended direct-driven spindle using neural network inverse scheme. *Mech. Syst. Signal Process.* **2017**, *88*, 36–48. [CrossRef]
22. Sun, X.; Xue, Z.; Zhu, J.; Guo, Y.; Yang, Z.; Chen, L.; Chen, J. Suspension force modeling for a bearingless permanent magnet synchronous motor using Maxwell stress tensor method. *IEEE Trans. Appl. Supercond.* **2016**, *26*, 0608705. [CrossRef]
23. Sun, X.; Jin, Z.; Cai, Y.; Yang, Z.; Chen, L. Grey wolf optimization algorithm based state feedback control for a bearingless permanent magnet synchronous machine. *IEEE Trans. Power Electron.* **2020**, *35*, 13631–13640. [CrossRef]
24. Werfel, F.N.; Floegel-Delor, U.; Riedel, T.; Rothfeld, R.; Wippich, D.; Goebel, B. HTS magnetic bearings in prototype application. *IEEE Trans. Appl. Supercond.* **2010**, *20*, 874–879. [CrossRef]
25. Sun, X.; Chen, L.; Jiang, H.; Yang, Z.; Chen, J.; Zhang, W. High-performance control for a bearingless permanent magnet synchronous motor using neural network inverse scheme plus internal model controllers. *IEEE Trans. Ind. Electron.* **2016**, *63*, 3479–3488. [CrossRef]
26. Zhu, R.; Xu, W.; Ye, C.; Zhu, J.; Lei, G.; Li, X. Design optimization of a novel heteropolar radial hybrid magnetic bearing using magnetic circuit method. *IEEE Trans. Magn.* **2018**, *54*, 8201105. [CrossRef]
27. Ye, X.; Le, Q.; Zhou, Z. A novel homopolar four degrees of freedom hybrid magnetic bearing. *IEEE Trans. Magn.* **2020**, *56*, 6703404. [CrossRef]
28. Ye, X.; Le, Q. Suspension force analysis on novel heteropolar four degrees of freedom hybridmagnetic bearing. In Proceedings of the 2020 IEEE International Conference on Applied Superconductivity and Electromagnetic Devices (ASEMD), Tianjin, China, 16–18 October 2020; pp. 1–2.
29. Ji, L.; Xu, L.; Jin, C. Research on a low power consumption six-pole heteropolar hybrid magnetic bearing. *IEEE Trans. Magn.* **2013**, *49*, 4918–4926. [CrossRef]
30. Wang, K.; Wang, D.; Lin, H.; Shen, Y.; Zhang, X.; Yang, H. Analytical modeling of permanent magnet biased axial magnetic bearing with multiple air gaps. *IEEE Trans. Magn.* **2014**, *50*, 8002004. [CrossRef]
31. Zhu, R.; Xu, W.; Ye, C.; Zhu, J. Novel heteropolar radial hybrid magnetic bearing with low rotor core loss. *IEEE Trans. Magn.* **2017**, *53*, 8210305. [CrossRef]